Coulomb drag propulsion experiments of ESTCube-2 and FORESAIL-1

Iaroslav Iakubivskyi[a,b], Pekka Janhunen[c], Jaan Praks[b], Viljo Allik[a], Kadri Bussov[d], Bruce Clayhills[b], Janis Dalbins[a], Tõnis Eenmäe[a], Hendrik Ehrpais[a,d], Jouni Envall[c], Sean Haslam[c], Erik Ilbis[a], Nemanja Jovanovic[b], Emilia Kilpua[e], Joosep Kivastik[a], Jürgen Laks[a], Philipp Laufer[f], Maido Merisalu[a], Matias Meskanen[c], Robert Märk[a,d], Ankit Nath[b], Petri Niemelä[b], Mart Noorma[a], Muhammad Rizwan Mughal[b], Samuli Nyman[b], Mihkel Pajusalu[a], Minna Palmroth[e,c], Aditya Savio Paul[a], Tatu Peltola[b], Mathias Plans[a], Jouni Polkko[c], Quazi Saimoon Islam[a], Anu Reinart[a], Bagus Riwanto[b], Väino Sammelselg[a], Janis Sate[g], Indrek Sünter[a], Martin Tajmar[f], Eija Tanskanen[b], Hans Teras[a], Petri Toivanen[c], Rami Vainio[h], Mika Väänänen[e], Andris Slavinskis[b,a]

[a] *University of Tartu, Ülikooli 18, 50090 Tartu, Estonia*
[b] *Aalto University, Maarintie 8, 02150 Espoo, Finland*
[c] *Finnish Meteorological Institute, Erik Palménin aukio 1, 00560 Helsinki, Finland*
[d] *Estonian Student Satellite Foundation, W. Ostwaldi 1, 50144 Tartu, Estonia*
[e] *University of Helsinki, Gustaf Hällströmin 2, 00560 Helsinki, Finland*
[f] *Dresden University of Technology, Institute of Aerospace Engineering, Marschnerstraße 32, 01307 Dresden, Germany*
[g] *Ventspils University of Applied Sciences, Inženieru 101, LV-3601 Ventspils, Latvia*
[h] *University of Turku, Vesilinnantie 5, 20014, Finland*

Abstract

This paper presents two technology experiments – the plasma brake for deorbiting and the electric solar wind sail for interplanetary propulsion – on board the ESTCube-2 and FORESAIL-1 satellites. Since both technologies employ the Coulomb interaction between a charged tether and a plasma flow, they are commonly referred to as Coulomb drag propulsion. The plasma brake operates in the ionosphere, where a negatively charged tether deorbits a satellite. The electric sail operates in the solar wind, where a positively charged tether propels a spacecraft, while an electron emitter removes trapped electrons. Both satellites will be launched in low Earth orbit carrying nearly identical Coulomb drag propulsion experiments, with the main difference being that ESTCube-2 has an electron emitter and it can operate in the positive mode. While solar-

wind sailing is not possible in low Earth orbit, ESTCube-2 will space-qualify the components necessary for future electric sail experiments in its authentic environment. The plasma brake can be used on a range of satellite mass classes and orbits. On nanosatellites, the plasma brake is an enabler of deorbiting – a 300-m-long tether fits within half a cubesat unit, and, when charged with −1 kV, can deorbit a 4.5-kg satellite from between a 700- and 500-km altitude in approximately 9–13 months. This paper provides the design and detailed analysis of low-Earth-orbit experiments, as well as the overall mission design of ESTCube-2 and FORESAIL-1.

Keywords: Coulomb drag propulsion, plasma brake, space debris, deorbiting, electric solar wind sail, ESTCube-2, FORESAIL-1, space sustainability

---

Acronyms

ADCS Attitude Determination and Control System. 10, 31, 33, 35, 38

ADR Active Debris Removal. 6, 7

AOCS Attitude and Orbit Control System. 23, 24, 27, 28

ATOX ATomic OXygen. 12, 22, 30

CDP Coulomb Drag Propulsion. 7–14, 16–19, 22, 24, 26, 28, 32, 33, 35, 38–40

CGP Cold-Gas Propulsion. 22, 24, 26, 38

CMOS Complementary Metal-Oxide Semiconductor. 26, 29

CNT Carbon NanoTube. 15

COM COMmunication system. 28

COTS Commercial Off-The-Shelf. 16, 29

CRE Corrosion-Resistance Experiment. 28, 30

CSP Cubesat Space Protocol. 28

EOP Earth-Observation Payload. 29

EPS Electrical Power System. 28, 35

ESA European Space Agency. 6

ESEO European Student Earth Orbiter. 29

FCC Federal Communication Commission. 5

FoV Field of View. 26, 27, 29

FPGA Field-Programmable Gate Array. 22, 26, 29

GPS Global Positioning System. 27

GS Ground Station. 27, 28

HSCOM High-Speed-COMmunication system. 29

ICP Internal Communication Protocol. 28

LEO Low Earth Orbit. 5, 6, 8, 9, 12, 15, 19, 26, 31, 39

MCU MicroController Unit. 16, 27, 28, 35, 36

MPPT Maximum Power Point Tracking. 35

OBC On-Board Computer. 11, 28, 35

PATE PArticle TElescope. 31, 32, 35, 36

PMD Post-Mission Disposal. 6, 7

RF Radio Frequency. 20, 22, 27

RW Reaction Wheel. 22, 24–26

SDR Software Defined Radio. 22, 29

SGP Simplified General Perturbation. 19, 20, 28

SP Side Panel. 28

SRAM Static Random-Access Memory. 28

SRM Spin-Rate Modification. 10, 19

ST Star Tracker. 23, 26–29

TM Tip Mass. 9, 12, 13

UHF Ultra-High Frequency. 35

ULF Ultra-Low Frequency. 37

1. Introduction

The era of artificial satellites began in the middle of the 20^{th} century with the launch of the first object into orbit [1]. The Space Era provided fascinating opportunities to bring new technological, social, economic, and safety (military/defence) aspects into people's lives. However, along with these opportunities, it also brought uncontrolled man-made space objects, the quantity of which is presently rapidly growing. Consequently, the risk of collisions with functional satellites is increasing. Moreover, it also creates the risk of uncontrolled re-entry of upper-stage rockets, final-stage vehicles, satellites, and parts of these over-populated or industrial areas. In the cases of heavy and large enough objects, or those made out of materials with high melting temperatures, the probability of surviving travel through Earth's atmosphere is considerable [2].

A study by the Inter-Agency Space Debris Coordination Committee has shown that the population of space debris will increase due to collisions, even if

nothing new is launched [3]. Each collision can create thousands of new items of debris that will consequently result in more collisions. This phenomenon is known as the Kessler syndrome. Collisions equivalent to the tragic one between Cosmos 2251 and Iridium 33 are predicted to take place every five to nine years [4]. More evidence comes from the recent collision of a centimetre-sized particle with a solar panel on the Sentinel-1A satellite [5].

New missions are being developed and will be launched in the upcoming years, and the launching of spacecraft fleets and constellations will continue. A number of private companies obtained licensing from the Federal Communication Commission (FCC) to launch thousands of global internet-provision satellites to non-geostationary-satellite orbits. While there are no doubts about democratisation of information and global internet access benefiting society, these constellations are planned to be accommodated in Low Earth Orbit (LEO) which raises the question of the future sustainability of the LEO environment [6, 7]. For instance, the simulations of the proposed constellations by OneWeb (720 satellites at 1200-km altitude) and SpaceX (1664 satellites at 1150-km altitude) give a probability of one dramatic collision every five years with probabilities of 5% and 45.8%, respectively [8]. A SpaceX Starlink constellation might reach 4425 satellites in orbital planes varying between 1100 km (inclination 53.8°) and 1325 km (inclination 70°) [9]. SpaceX's most recent revised plan, which was submitted to the FCC, requested 1500 satellites to be operational at 550 km, and the latest request was approved for an additional 7518 satellites in altitudes between 335 km and 348 km [10], which in some ways represents the company's awareness of the space debris issue.

The fact that the launching cost of nano- and picosatellites is typically higher than building them has escalated an enormous interest in low-cost small launch vehicles. Around 40 emerging small booster systems with payload capacities ranging from 5 kg to 800 kg are under development, and some are currently operational [11]. About the same number of launch vehicles are either in the study phase or public information about them is absent [11]. The trend indicates the global market's need to launch a single or small number of flight-sharing

smallsats into LEO. The estimated cost per kilogram varies between €10k and €68k [11], but the goal is to reduce this further, which might increase demand in the launch market.

Aforementioned facts indicate the elevated probability of a radical increase in space debris population in LEO. The issue of ever-increasing debris is regulated by the limited orbital post-mission lifetime of 25 or 30 years after launch for all satellites in LEO [12]. Debris prevention guidelines are under development by the United Nation's Committee on the Peaceful Uses of Outer Space; however the policies are not legally binding. Furthermore, recommendations have not been adopted at the national level; thus there is, to date, no effective mechanism to globally control the future growth of space debris.

Many space debris mitigation techniques have been proposed in recent years. Present and potential space junk can be fought off by a Post-Mission Disposal (PMD) device included on board a satellite, or by Active Debris Removal (ADR) concepts [13] by employing a dedicated satellite or a system to deorbit non-functional objects. Alternative futuristic ideas are built on recycling valuable materials (e.g., aluminium, titanium, solar panels, empty tanks) by delivering them to the vicinity of human space camps on Mars or other planetary bodies.

The PMD of a satellite can be achieved by lowering orbital altitude with further burning in the upper stages of the atmosphere, or by controlled re-entry. In rare cases, removal can be achieved by the manoeuvring of the satellite to disposal orbits above LEO or geosynchronous orbit. However, when accounting for potential future large constellations, even with 90% PMD success, the population of debris will still grow in the long term and with 50% PMD will provide a catalyst for detrimental population increase [6]. Hence, the need to eliminate further increase of nonfunctional objects is obvious. Any mission that potentially creates a risk of increasing the debris population should include PMD means and bed designed for demise when applicable [14, 15].

Among ADR capturing techniques are nets, harpoons, robotic arms with a clamping mechanism, contactless deorbiting via employment of an ion beam, and magnetic capture mechanisms. The European Space Agency (ESA) e.Deorbit

mission is planning to test a net/harpoon-based ADR on a nonfunctional 62.5 m^3 Envisat satellite in 2023 [16, 17]. Recently, the RemoveDEBRIS mission showed successful in-orbit harpoon and net utilisation [18]. Commercial deorbiting services can potentially be executed by companies like *D-Orbit* and *Astroscale*.

Conventional PMD can be achieved by implementing propulsion, for instance electrical (which has a high power consumption) or chemical (which is heavy). Such solutions would require a fully functional satellite at the end of the mission. Alternative PMD deorbiting concepts may be competitive options compared to conventional propulsion systems in terms of required mass fraction [19]. Among proposed novel and alternative methods are passive and active electrodynamic drags [20], deorbiting sails [21], parachutes [22] and Coulomb Drag Propulsion (CDP) plasma brake deorbiting [23, 24]. Relatively thick electrodynamic tethers create a high risk of collisions. The aerodynamic sail has a complicated deployment system and can be easily damaged by micrometeoroids and subsequently increase the amount of small debris. The sustainability of the aerodynamic brake has to be considered because the method does not decrease the area–time product, and hence it might not lower the probability of collisions [25]. The CDP plasma brake is a lightweight, small, scalable and effective deorbiting concept. Moreover, it is safe for other space assets, even if an unavoidable collision with the tether occurs. However, the CDP has not yet been demonstrated in orbit. A simplistic overview of deorbiting systems in shown in Figure 1.

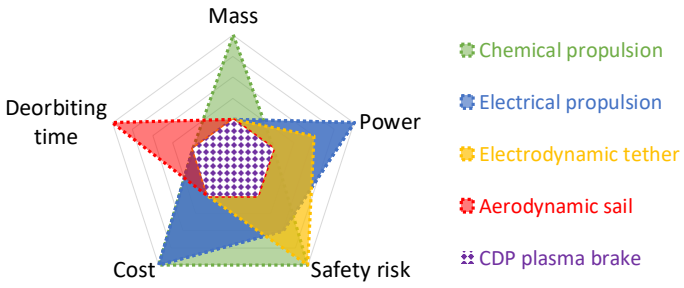

Figure 1: Simplistic comparative overview of deorbiting modules. The CDP is the pentagon in the middle.

The first voyage of the CDP experiment to LEO was on board the ESTCube-1 and then Aalto-1 satellites. ESTCube-1 was operated until 2015 without successful tether deployment, possibly due to the reel being jammed or failed reel-lock release [26]. Aalto-1 [27] is currently active in orbit as of June 2019, and the tether deployment experiment has commenced and is ongoing. ESTCube-2 and FORESAIL-1 represent a new generation of CDP satellites which follow the troubleshooting philosophy of their ancestors. Historically, tether deployment in space is a challenging task [28].

Here we present CDP for deorbiting in LEO on two upcoming cubesat missions – ESTCube-2 and FORESAIL-1. The paper is organised as follows. Section 2 presents the experiment design, requirements, deployment method, and the tether design. Section 3 shows the system performance and risk assessments. Sections 4 and 5 provide descriptions of ESTCube-2 and FORESAIL-1 architectures, respectively, and present other payloads. Section 6 provides information about the possible scaling and alternative applications of CDP. Conclusions are provided in Section 7.

2. Experiment requirements and design

The CDP experiment is being developed at the Finnish Meteorological Institute. The purpose of the experiments is to deploy a long, thin tether, bias it to a high voltage with respect to the atmospheric plasma, and measure the resulting Coulomb drag. The voltage is negative, but on ESTCube-2 a positive mode experiment is also being carried out. For deorbiting in LEO, the negative voltage mode is the baseline choice because it requires less power and does not need electron emitters. As shown in Figure 2, when negatively charged, the CDP tether serves as a plasma brake that lowers the spacecraft orbit. For electric sailing in the solar wind [29], positive voltage is preferred because it enables a higher voltage to be used and does not have a significant interaction with photoelectrons [30].

The spacecraft is spun to stretch the tether with a centrifugal force, which

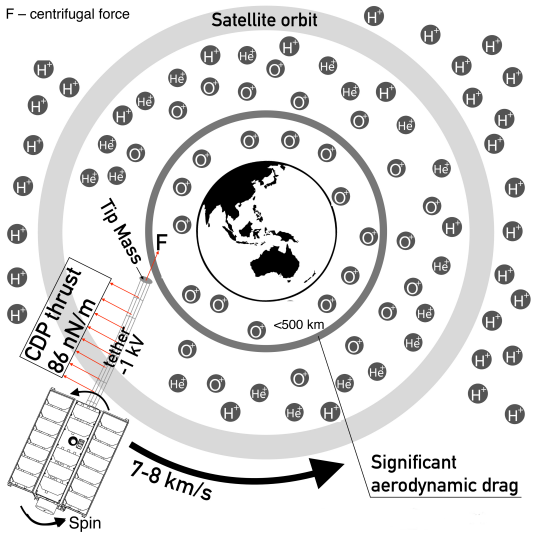

Figure 2: Operational visualisation of CDP-based deorbiting in LEO. Maximum thrust is achieved when the tether is perpendicular to the plasma ram flow.

dominantly applies to Tip Mass (TM). Deployment is assisted by tether reel rotation, which itself is activated by a motor. Movement of the tether away from the satellite during deployment causes a decrease in spin rate. Deployment is periodically paused so that the rotation can be accelerated. The spin rate is adjusted so that the tether tension remains within permissible bounds: exceeding 0.3 cN to pull out the tether but not reaching the 3 cN tension limit which might break the tether. In the case of ESTCube-2, the positive mode experiment sequence will be carried out at a few tens of metres' length, because when biased at high, positive voltage, a longer tether would gather more electron current than the experimental on-board electron emitter can provide. After deployment, the tether is still tensioned by spinning. We measure the Coulomb drag force by turning on and off the tether voltage in sync with the rotation and measuring the resulting change in the spin rate. Independently, we can also determine the CDP thrust from the lowering of the orbital altitude.

2.1. Requirements

The CDP experiment should support two modes of operation:

1. Spin-Rate Modification (SRM) when the tether is charged either positively or negatively in synchronisation with the satellite's rotation: the spin rate increases when moving downstream and decreases when moving upstream. The change in spin rate during one polar pass is expected to be $\approx$0.1 deg·s^{-1} for the CDP negative mode; for the positive mode it is expected to be $\approx$0.06 deg·s^{-1}. For more details see Subsection 3.1.
2. Deorbiting with the plasma brake when the tether is continuously charged negatively. It is estimated that the satellite will deorbit by 10 km in six months with an unwrapped 30-m tether. Effective deorbiting requires at least 150 m of deployed tether. For more details see Subsection 3.1.

The CDP payload should perform the following operations:

1. Reel out the tether at $\sim$1 mm·s^{-1}.
2. Charge the tether negatively.
3. On board ESTCube-2, charge the tether positively and remove electrons.
4. Turn the charging on and off in a seconds-long time frame (SRM mode).
5. Provide an angular momentum to deploy at least 30 m of the tether (preferably all 300 m) starting from the initial 11 m, for which the angular momentum is provided by the Attitude Determination and Control System (ADCS).
6. Keep the tether charged for a period of at least six months (deorbiting mode).

The ADCS should support the CDP experiment with the following functions:

1. Provide enough angular momentum to deploy the first 11 m of tether without additional spin-up manoeuvres. The spin axis should be aligned with the Earth's polar axis with a pointing error of less than 3°.
2. Provision of additional angular momentum by the ADCS is optional. If it is provided, the tether deflection angle (between the tether and the normal of the satellite's surface) should be less than 15°.
3. Provide on and off signals for charging the tether in synchronisation with the satellite spin.

4. Keep the tether tension between 0.3 and 3 cN.
5. Estimate a change in the magnitude of angular velocity of at least 0.1 deg·s^{-1} over 900 s (approximately two polar passes).
6. Estimate a change in the orbital altitude of at least 10 km over six months.

The satellite platform should support the CDP experiment as follows:

1. Host the module of 0.5 kg and half a cubesat unit at one end of the longitudinal axis.
2. Align tether's attachment point with satellite's centre of mass along two short axes if possible.
3. Provide 7 W of peak power during tether deployment (can be performed with a low-duty cycle).
4. Provide 0.6 W of continuous power.
5. Provide experiment control and data interface with the On-Board Computer (OBC).

2.2. Tether

The tether consists of several conducting wires that are bonded to each other to produce a redundant structure that withstands micrometeoroid impacts in space. As a single wire would be cut in a matter of days in orbit, a tether can be engineered to have a desired lifetime under the expected micrometeoroid flux. The thickness of the individual wires and the number of wires are dictated by the applied tether voltage and the electron density of the given plasma environment. The larger the surface area of the tether wires, the larger the electron current the positive tether gathers. This dictates the mass of the high-voltage power system that maintains the tether voltage. The wire thickness is expected to be 30–50 μm. In the case of gold, a 300-m-long tether will weigh approximately 26 g, and about 2 g in the case of aluminium.

Two types of tethers and manufacturing processes are being developed for the CDP. One is based on the diffusion bonding of either silver or gold wires. The resulting tether has a few parallel wires and perpendicular wires resembling

rungs in a ladder, which creates a multi-cell structure [31]. In LEO, silver is not an optimal material due to fast erosion caused by ATomic OXygen (ATOX). Gold and aluminium can resist ATOX. The absence of an oxide layer on gold runs the risk of the cold welding during the launch. An alternative tether type is the "twisted wiring" method where individual bonds are made by twisting wires around each other to produce a mesh (analogous to "chicken wire" used in farming). This type of bond sets no limitation to the metal alloys that can be used for tether production. While the method is widely used and robust for everyday mesh and wire dimensions, it has not yet been demonstrated for wires in the μ-metre range or mesh sizes in the centimetre range. Recently, we demonstrated the twisting method for the CDP tether dimensions at the proof-of-concept level using a manually operated machine.

2.3. Deployment system

The key components of the tether deployment system are the tether reel, the tether chamber, the stepper motor, and the TM, shown in Figure 3. The stepper motor is nested inside the tether reel, thereby avoiding any gearbox complexity. The motor speed can be varied by microstepping to obtain a suitable out-reeling speed for the tether and its TM. The tether reel and the motor are enclosed in a chamber that has an opening for the TM. The opening is located on a short side panel of the satellite so that the TM is already in free space after its launch locks have been burned. The TM serves as an auxiliary mass to keep the tether stretched. It has a button-like shape, with the flat side being perpendicular to the tether. The TM is a few centimetres in diameter, is made out of an aluminium alloy, and weighs approximately 2–2.5 g.

The chamber has three functions: to reduce the pull required for tether deployment during the out-reeling, to shield the rest of the payload from the high-voltage reel, and to shield the satellite from any broken tether fragments should the tether break during the launch.

The diagnostics of the tether's deployment systems consist of optical sensors that monitor the state of the launch locks and the status of the TM. There are

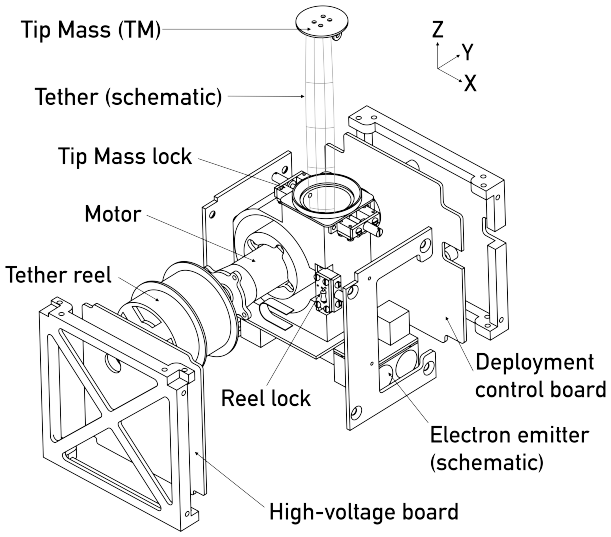

Figure 3: Coulomb drag payload assembly. Coordinate system is in accordance with Figure 8.

two separate launch locks for the TM and a reel lock, which keeps the reel from turning during payload integration and launch. They are released during the commissioning phase. The TM monitoring systems are based on near-infrared light-emitting diodes and photo transistors.

The tether is angularly deflected from its nominal radial direction during the reel-out stage. The deflected angle increases as a function of the deployment speed. The deployment speed is determined by the satellite spin rate and the mass of the TM. The required out-reeling speed for ESTCube-2 and FORESAIL-1 is $\sim$1 mm$\cdot$s^{-1}.

2.4. High-voltage source

Two high-voltage sources are being developed for the CDP experiments. For the plasma brake, the source provides a voltage of about -1 kV (negative mode). A positive voltage source can be tuned with a maximum voltage of $+5$ kV for the CDP experiment. The positive voltage is only applied in ESTCube-2 which is expected to have two types of electron emitters. One is the cold cathode emitter introduced in Section 2.5. The other is a traditional hot cathode, which

is used, for instance, in scanning electron microscopes. Grounding schemes for both positive and negative CDP modes are shown in Figure 4. Note that the cathode of the emitter is grounded to the satellite chassis, and only the tether is at a high voltage.

Two high-voltage converters are used to run the electron guns in the positive mode. The primary converter will be used for charging the tether. The secondary converter will be implemented to the electron emitter assembly for electron extraction (cold cathode) and acceleration. Its voltage can be adjusted from 0.5 to 2.0 kV. For the hot cathode gun, 0.5 kV is applied to kick the electrons through the potential well of the tether. To extract the electrons from the cold cathode, a voltage of about 2.0 kV is required. Both converters are tunable; the emitter converter can be used to vary the electron current, and the tether converter can be used for measuring the Coulomb drag as a function of the applied voltage.

For the negative mode, no ion emitter is required, as the ion current to the tether is much smaller than the electron current in the case of positive voltage. The primary converter generates a potential difference between the tether and a conducting surface area, which can be, for example, the satellite's frame (ESTCube-2) or a deployable boom (FORESAIL-1). The conducting area then collects electrons while in equilibrium. This settles to a low positive potential with respect to the plasma, and the tether is maintained in the desired negative potential.

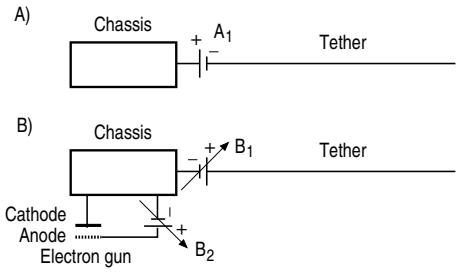

Figure 4: Schematic of the grounding for negative (A) and positive (B) CDP experiments. Negative mode includes one converter and positive mode requires at least two.

2.5. Electron emitter

Initially, the electron emitter was developed at Dresden University of Technology as a neutraliser for the NanoFEEP propulsion system, which is a miniaturised field emission electric propulsion thruster for small satellites. In order to prevent spacecraft charging due to the emitted ion current, an electron source with low power consumption is needed. A one-unit cubesat of the University of Würzburg (UWE4) with four thrusters and two neutralisers was launched in December 2018 and has been operational in LEO orbit since February 2019 [32]. As a spin-off, the electron source will be applied in the ESTCube-2 satellite. The miniaturised electron source, with a footprint of only 15×13 mm^2, is based on technology used for cold-field emission of multi-walled Carbon NanoTubes (CNTs), shown in Figure 5. The CNTs were grown by chemical vapour deposition and consist of multiple concentric tubes of arranged single-layer carbon atoms that provide intense electrical-field enhancement due to their high aspect ratio. Additionally, the nano-material is chemically inert, insensitive to ambient pressure and contamination, highly electrically conductive, stable at high temperatures, and has a relatively low work function. These characteristics make it ideal for application in a high-performance, low-power-consuming, cold electron source for space applications [33]. For laboratory experiments, a triode configuration with only one electrical potential between -500 V and -3 kV within the CNT material is established (Figure 5). The extractor and the collector are kept at ground potential while a continuous electron current is emitted by the CNT-material. Therefore, the electrical potential of the emitter slightly fluctuates, due to the inconsistency in the direction of electron emission. The alignment of the individual components and the mechanical design leads to a high transmissivity of 75 to 90% so that the electron losses at the extractor remain small. Long-term experiments, up to 500 h continuous operation at 120 μA emission current, have demonstrated high emission stability with low degradation. Relative to the distance between the CNT material and the extractor, an ignition potential of 500 V to 800 V is implemented, while the proposed current limit of 0.5 mA is reached at 1.5 kV.

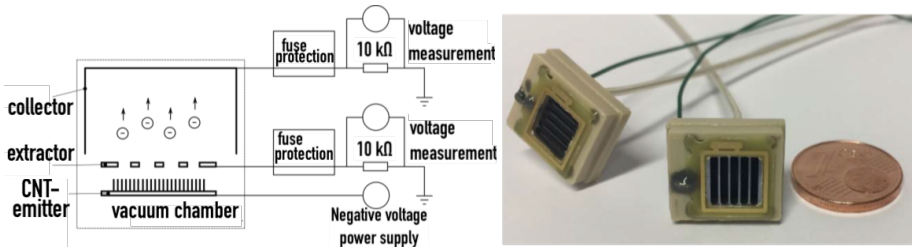

Figure 5: Schematic illustration of the experimental arrangement (left) and photograph of the miniaturised cold electron source (right) compared to a one-€-cent coin.

2.6. Deployment electronics

A two-phase bipolar stepper motor, *phy*SPACE 19 (from *Phytron*), was chosen for the tether-reel motor and will be used on ESTCube-2 and FORESAIL-1. A stepper motor is the preferred choice, as it provides precise positioning and high torque, while remaining robust enough for space applications. The stepper motor integrates two embedded thermocouples to provide accurate temperature readings of motor windings.

The motor is driven by a Commercial Off-The-Shelf (COTS) DRV8834 integrated circuit driver from *Texas Instruments*. The circuit implements microstepping, over-temperature lockout, and over-current and under-voltage protection.

The motor power will be provided by a 5-V line that is regulated from the battery voltage by two LTC3603 buck regulators. The nominal power consumption of the payload is continuously about 7 W during reeling operations. However, the reel-out process will be executed during a multi-stage process with a few spin-up manoeuvres to compensate for changes in spin rate and to provide the required pull force. Thus, the total power consumption during reel-out is flexible, and the exact execution procedure will be decided depending on the available power.

An optical rotary encoder circuit will be used to track rotation speed and positioning of the stepper motor. Control of deployment electronics will be dealt with by the CDP-experiment MicroController Unit (MCU).

3. Performance estimation

3.1. Coulomb drag propulsion performance

The CDP plasma brake deorbiting technique taps momentum from the ionospheric plasma by employing a long, thin and conductive tether that is attached to the disposal object. The disposal object is typically an artificial satellite at the end of its mission. The satellite moves through relatively immobile (in comparison to the 7–8 km·s^{-1} orbital speed) ionospheric plasma, and if the tether is charged negatively, there results an interaction force between the tether and the plasma ram flow, known as CDP plasma brake [23]. The Coulomb friction slowly brakes the satellite orbital speed, consequently lowering the orbital altitude.

A previous particle-in-cell simulation study obtained the thrust per unit length calculation for a CDP plasma brake, which is given in Equation 1 [34].

$$\frac{dF}{dz} = 3.864 \times P_{dyn}\sqrt{\frac{\epsilon_0 \tilde{V}}{e\ n_0}} exp(-\frac{V_i}{\tilde{V}}) \tag{1}$$

where $P_{dyn} = m_i n_0 v_0^2$ is the dynamic pressure, m_i is the ion mass, and v_i is the plasma flow with respect to the satellite; $\tilde{V}$ is given in Equation 2.

$$\tilde{V} = \frac{V_w}{\ln(\lambda_D^{\text{eff}}/r_w^*)} \tag{2}$$

where r_w^* is the effective electric radius of tether, $\lambda_D^{\text{eff}} = \sqrt{\epsilon_0 V_w / e n_0}$ is the effective Debye length and $V_i = m_i v_0^2/2e$ is the bulk ion flow energy.

Using Equation 1 for the negative CDP experiment, the thrust per unit length is approximately 86 nN·m^{-1}, considering the tether's width of 2 cm, the single-wire diameter of 35 μm, the mean ion mass of 10 amu, and a -1-kV voltage for the tether. However, the assumption is made for the ideal case where the plasma ram flow is always perpendicular to the tether. In reality, we expect 50–75% of the thrust value due to variations in the spin plane in relation to the orbital vector. This means that, in some cases, for 25–50% of orbital time, the tether will be nearly parallel to the satellite motion vector, resulting in near-zero

thrust. Hence, the final deceleration calculation requires an additional attitude factor varying between 0.5 and 0.75. This number requires further correlative testing with flight results.

Resulting deorbiting rates for a typical three-unit cubesat (4.5 kg, which approximately corresponds to ESTCube-2 and FORESAIL-1) are shown in Figure 6. The rate is assumed exclusively based on the CDP effect for various deployed lengths. The atmospheric drag will also contribute to deorbiting, though this is not included in these calculations. Due to uncertainties in the exact attitude factor, the graph includes wide uncertainty ranges for each tether length.

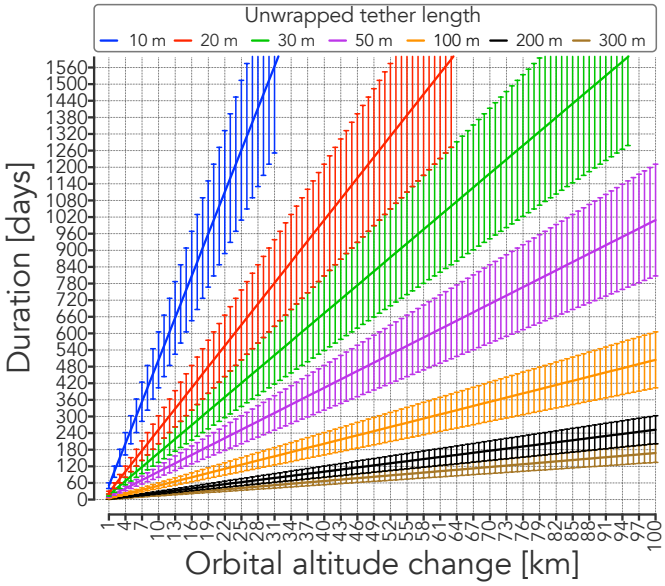

Figure 6: Expected deorbiting rates by the CDP for a three-unit cubesat (4.5 kg) with various unwrapped tether lengths.

Besides technological limitations and engineering implementations, there are environmental factors that play a role in Equation 1 and are hard to predict. These factors include (i) ionospheric plasma density and distribution, and (ii) the ion ratio of oxygen to hydrogen. Ionospheric plasma is distributed in a somewhat chaotic manner at various latitudes, longitudes and altitudes, and it also migrates. Migration is enhanced by solar activity. Hence, the prediction in

Figure 6 might have some deviations, depending on space weather.

Technology for positive CDP, widely known as the electric solar wind sail, will be tested in the same environment. While the most effective way to use the electric sail is in the solar wind domain as primary propulsion, the main objective in LEO is to estimate the thrust of the system. The positive CDP tether will interact with ionospheric plasma, resulting in a change in spin rate. The measured change will provide an estimation of the thrust value. The thrust per unit tether length for CDP positive mode in LEO is expected to be 57 nN·m^{-1} for the ESTCube-2 system.

SRM mode is implemented when the tether is charged either positively or negatively in synchronisation with satellite rotation: the spin rate increases when moving downstream and decreases when moving upstream. See Section 2 of [35] for more details. By using Equation 1 of [35], it is estimated that the change in spin rate during one polar pass will be ≈0.1 deg·s^{-1} and ≈0.06 deg·s^{-1} while running the CDP experiment in negative and positive modes, respectively. We have assumed the arm length to be 5.5 m (≈11 m of tether deployed for the initial experiment); the expected CDP force to be 86 nN·m^{-1} and 57 nN·m^{-1} in negative and positive modes, respectively; the tether to be charged 1/3 of the time during a polar pass (i.e., either going downstream or upstream and having a 30° safety margin); the polar pass to last for 470 s; and the moment of inertia to be 0.35 kg·m^2. Such a tether length is set by keeping the tether tension within the 0.3 and 3 cN limits and deploying the maximum tether length with a single spin-up manoeuvre (see Subsection 5.1). The experiment can continue with a longer tether (up to 300 m) whose deployment requires an additional angular momentum, which can be provided either by an attitude control system (as with the initial spin-up) or using the CDP itself in the case that the SRM experiment is successful.

The actual deorbiting rate with an 11-m tether in a reasonable time frame (e.g., half a year) is about 3 km, which is challenging to verify with the Simplified General Perturbation (SGP)-model measurement [36]. Using Equation 1, we estimate that the satellite would deorbit by 10 km in half a year, with 30 m of

the tether out and assuming a 0.5 attitude factor (i.e., the worst-case scenario, when the tether is perpendicular to the plasma ram flow for only half the orbital time). Such an altitude change can be estimated with the SGP model and, therefore, at least 30 m of the tether is required to be deployed. In order to demonstrate the plasma brake for effective deorbiting (i.e., useful for operational missions after their lifetime), at least 150 m of the tether should be unwrapped. Such a length would secure a 10-km-per-month deorbiting rate.

ESTCube-2 will be able to measure the orbital change by employing Radio Frequency (RF) ranging, as described in Subsection 4.3, and FORESAIL-1 will achieve this by retroreflector laser ranging, as described in Subsection 5.2.

3.2. Risk assessment

The mission failure risks concern the malfunction of a deployment mechanism or high-voltage source, insufficient or excessive centrifugal force for deployment, or the tether being damaged or cut by micrometeoroids or already-existing space junk. While most risks are handled by engineering solutions, the tether is more vulnerable to natural factors, which will be considered here.

In the case of the ESTCube-2 and FORESAIL-1 tethers, the 10-μm and 3-cm impact fluxes are relevant, as the first is a hazard to the single tether's wires, and the second impactor is capable of cutting the entire tether in one go (Figure 7). A typical 2-cm-wide and 300-m-long tether has an area of $A_t = 6$ m^2. According to the MASTER-2009 model version 7.02 for the year 2025, meteoroid and debris fluxes at an 800-km altitude (which is one of the most populated regions) for 3-cm and 10-μm impact fluxes are equivalent to $\Phi_1 = 1.6\text{e}{-5}$ m^{-2} per year and $\Phi_2 = 328$ m^{-2} per year, respectively. This results in $P_{t/1} = A_t \times \Phi_1 = 9.6\text{e}{-5}$ (0.0096%) single-blow breaking probability per year or $P_{t/2} = 1.92\text{e}{-4}$ (0.0192%) per two years – the duration of the mission. A single wire's surface area is $A_w = 1.08\text{e}{-5}$ m^2 with a corresponding fatal flux of Φ_2. The breaking probability of the tether's single wire is $P_{w/1} = A_w \times \Phi_2 \approx 3.5\text{e}{-3}$ (0.35%) per year or $P_{w/2} \approx 7\text{e}{-3}$ (0.7%) for the mission duration. Taking into account the tether's four segments (Figure 7),

the breaking probability per tether's cell is equivalent to $P_{c/2} = P_{w/2}^4 = 2.4\text{e}{-9}$ within two years. If one assumes that cells are 10 cm long, a 300-m-long tether will have $N_c = 3000$ cells (see Subsection 2.2). This results in a total breaking probability of $P_{W/2} = N_c \times P_{c/2} = 7.2\text{e}{-6}$ ($7.2\text{e}{-4}\%$). Hence, the total breaking probability of such a tether is $P_{t/2} + P_{W/2} \approx 0.02\%$ over two years by 10-μm and 3-cm fluxes.

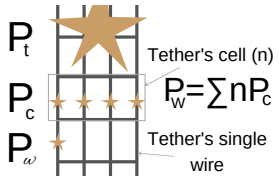

Figure 7: A schematic of tether's impact probabilities.

The safety risk is relevant to active space assets, since the system is quite large, considering the length of the deployed tether. If the tether or part of it were to collide with other spacecraft at orbital hypervelocity, no significant harm or damage to the object, the tether collides with, would occur. Linear scratches resulting from such an accident would be equivalent to ones that spacecraft experience constantly under nominal operation. Optical elements are typically protected by baffles. If the collision happens with solar cells, it might cause a short circuit via the conductive tether; however, it was estimated that the tether will evaporate in a hypervelocity impact [37]. The typical atmospheric density for a 600-km altitude is $2.4\text{e}{-13}$ kg·m^{-3}. Considering the tether's cross-sectional area and mass-per-length properties, the resulting acceleration is $1.3\text{e}{-4}$ m·s^{-2}. Decreasing the altitude by 200 km requires 100 m·s^{-1} delta-v, which is, by a conservative estimate, obtained in nine days in the case of an aluminium tether and two months in the case of a gold tether. The atmospheric density for an 800-km altitude is 11 times smaller than for 600 km. From an orbital altitude of 800 km, a loose tether piece deorbits passively in 3.3 months in the case of an aluminium tether and in two years in the case of a gold tether. Moreover, if passive electrodynamic and electrostatic effects, as well as the atmospheric

density function in relation to altitude, are taken into account, deorbiting time becomes even shorter.

4. ESTCube-2

The ESTCube-2 platform is being developed by devoted volunteers of the Estonian Student Satellite Foundation [38, 39]. Supervision, laboratories, integration and quality control are provided by Tartu Observatory, University of Tartu. The ESTCube-2 layout is shown in Figure 8. The satellite is planned to be launched in 2021. The focus of this paper is the satellite's main mission – to estimate the CDP force in the ionosphere in positive and negative modes and to demonstrate deorbiting with the plasma brake. ESTCube-2 has several technology demonstration experiments that are briefly described in this section.

- Demonstrate technologies of a highly-integrated nanospacecraft platform (one cubesat unit) which could be used for deep-space missions outside the Earth's magnetosphere – star tracker, Reaction Wheels (RWs), Cold-Gas Propulsion (CGP) and RF ranging. The CDP's positive mode would also provide propellantless means of propulsion in interplanetary space (electric solar wind sail).

- Demonstrate Earth observation with a multispectral imager (Tartu Observatory).

- Demonstrate high-speed communications with the Software Defined Radio (SDR)-type transceiver based on the Field-Programmable Gate Array (FPGA) (Ventspils University of Applied Sciences).

- Demonstrate shielding performance by nanostructured coating against ATOX, and multilayered material against radiation (Institute of Physics, University of Tartu).

- Demonstrate a miniature science-grade magnetometer.

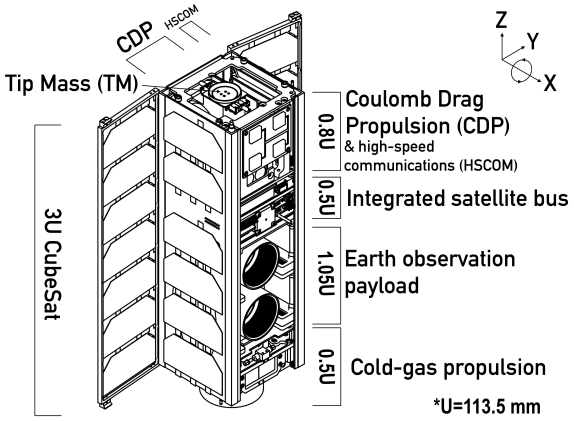

Figure 8: ESTCube-2 anatomy.

4.1. Attitude and orbit control system

The requirements for the ESTCube-2 Attitude and Orbit Control System (AOCS) are given in Subsection 2.1. While deployment of an 11-m tether within given tension limits requires about 130 deg·s^{-1} initial angular velocity (see Subsection 5.1 for more details), here we simulate a case of spinning up to 360 deg·s^{-1}. During the mission, the target spin rate can be easily limited, or a high spin rate can even be used if the tether turns out to withstand a higher tension. The satellite spin-up and pointing of the imager requires three-axis attitude determination, which, in turn, sets a high demand for on-board computations. Since the platform will be demonstrated for future use outside the Earth's magnetosphere, the use of magnetorquers and magnetometers is to be minimised.

ESTCube-2 attitude determination uses Sun sensors, gyroscopes, accelerometers and a Star Tracker (ST) with on-board magnetometers. See more details on the ST in Subsection 4.2. Sun sensors are developed in-house. Each Sun sensor consists of two single-row image sensors. Using a pair of two perpendicular single-row sensors, the complete Sun angle can be determined without the need for a matrix sensor, which helps to reduce the computational complexity. Four Sun sensors are placed on the satellite's large sides (+x, −x, +y and −y

shown in Figure 8). The sensor mask design is similar to the double-slit ones used on ESTCube-1 [40]; however, the analogue sensor has been replaced with a single-row image sensor S9226 (from *Hamamatsu*), which provides the ability to filter out the albedo and provide more accurate results.

The primary actuator of the satellite's attitude control system comprises three compact RW210 RWs (from *Hyperion Technologies*). The smallest versions will be used on-board ESTCube-2, and each will provide the satellite with 1.5 mN·m·s of momentum storage and 0.1 mN·m of torque.

ESTCube-2 is equipped with a CGP module NanoProp (from *GOMspace*). This 0.5-unit module provides a total of 40 N·s of momentum change via four thrusters located at the corners of the module on the −z side (Figure 8). The tank contains 50 g of liquid butane. Each of the thrusters has a resolution of 10 μN and can provide a maximum thrust of up to 1 mN. CGP will be used to desaturate RWs after spin-up manoeuvres, which is a critical functionality to test for future CDP missions.

The satellite hosts three-axis magnetorquers, which are manufactured in-house and are similar to the coils used on ESTCube-1 [40]. While ESTCube-1 employed coils as the primary means of attitude control, ESTCube-2 will minimise their use and keep them as a redundant backup option. The magnetorquers will mostly be used to desaturate the RWs when it is necessary to improve pointing capabilities.

A new Unscented Kalman filter has been developed for ESTCube-2. The filter combines measurements from multiple sensors to give an accurate prediction of the satellite's orientation, even if one or more of the redundant sensors cannot be used (e.g., Sun sensors during eclipse) or are malfunctional. The estimated attitude is, in turn, used by the various control algorithms that detumble, point or spin-up the satellite.

The aim of this preliminary study is to demonstrate that the ESTCube-2 AOCS can fulfil the spin-up-manoeuvre requirements, with a substantial margin to account for the limited scope of simulations. The simulation relies on the physical characteristics provided by the computer-aided design model of the

satellite. The satellite body, thruster system and RWs were combined into a single dynamic system. The friction of the RWs was assumed to be negligible during the simulation.

The spin-up manoeuvre is divided into three different parts akin to the different tasks of the control algorithms – detumbling, pointing and spin-up. An initial angular velocity of ≈6 deg·s^{-1} in every direction was introduced to demonstrate detumbling. After achieving a satisfactory stability of ≈6·10^{-4} deg·s^{-1}, the satellite was given a command to point its spin axis (+x) towards −y of the inertial reference frame. This serves as a simple substitute for any required axis. Afterwards, the satellite was commanded to spin-up along the acquired +x axis, up to an angular velocity of 360 deg·s^{-1}.

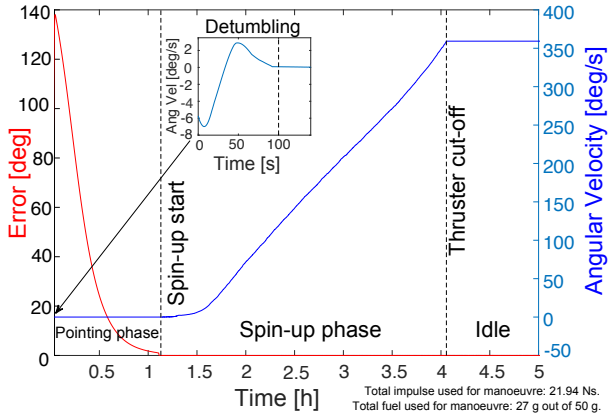

Figure 9: ESTCube-2 spin-up simulation. The red line shows the deviation of the satellite spin axis from the required heading. The blue line shows the angular velocity of the satellite around its spin axis.

As shown in Figure 9, the detumbling phase takes about 90 seconds to bring the satellite to a complete stop. The pointing phase then reduces the pointing error between its spin axis and the desired axis with 1 g of propellant. Pointing takes about an hour to conserve the propellant. The following spin-up phase takes about three hours and uses 26 g of propellant. After 360 deg·s^{-1} was achieved, the actuators were shut down, marking the completion of the manoeuvre. The final speeds for the +x, +y and +z RWs were 46, 10 and

-128 rad·s^{-1}, respectively, whereas the upper limit is $\approx$1100 rad·s^{-1}, meaning the RWs were nowhere close to saturating during such a spin-up manoeuvre.

4.2. Deep-space-technology demonstrations

The electric sail is well-suited to enable a mission with fleets of nanospacecraft, such as the Multi-Asteroid Touring concept [41]. However, several other technologies must be developed and demonstrated to enable such a radical change in interplanetary exploration: miniature RWs and CGP for attitude and spin control; miniature ST; optical navigation near a target and in deep space; communication solutions that would not rely solely on deep-space networks. Moreover, the components require characterisation with extended testing for a high-radiation environment and prolonged lifespan. As described in Subsection 4.1 and below, ESTCube-2 is taking the first steps in developing and testing such technologies in LEO. The ST functions can further be combined with near-target and deep-space optical navigation/orbit determination [42, 43, 44]. Without strict requirements for ranging with deep-space networks, an alternative communications approach can be envisioned [45].

The ESTCube-2 ST is being developed in-house from scratch. For the current mission, the ST serves as a source of high-accuracy attitude mostly required for pointing the imager. In missions outside the Earth's magnetosphere, the ST will provide the main attitude reference and can be used to track other objects when they are sufficiently bright. For example, if the CDP is to be demonstrated in lunar orbit (see Subsection 6.1 for more details), the ST can be used as an Earth and Moon sensor and for navigation purposes using planets of the Solar System at greater distances.

The ST uses an 1/2.5-inch MT9P031 monochrome Complementary Metal-Oxide Semiconductor (CMOS) image sensor (from *ON Semiconductor*) and a high-resolution imaging lens with 16-mm focal length and F/1.2 aperture for taking images of the stars. The combination of the sensor and optics yields a $21.5° \times 15.7°$ Field of View (FoV). The sensor is configured and read out by a Cyclone IV FPGA, that is also used to calibrate read-out data using dark

frames, and to detect the stars – their positions on the sensor's pixels and brightness. Detected stellar positions are sent to a STM32F401 MCU (from *STMicroelectronics*), where they are corrected for known optical distortions. After that, when true stellar positions are known, geometric patterns are created based on them, and patterns are matched to the stellar pattern hash catalogue using a geometric hash algorithm. A preprocessed star catalogue in the form of computed geometric hashes, containing information about stars up to a 5.5 magnitude, is stored on-board in a 256 Mb flash memory. After the identification of the stars, the coordinates of the centre of the FoV can be found. The expected accuracy, which corresponds to one pixel, is 28" or better. Celestial coordinates of the FoV, corresponding to the midpoint of exposure time, are sent to the AOCS for use in the Unscented Kalman filter. The nominal ST exposure time will be 0.1 s and the expected position-update frequency better than one second.

4.3. Radio-frequency ranging

The RF ranging experiment on-board ESTCube-2 is designed for a ground-based ranging topology, conceptualising a reverse Global Positioning System (GPS). The experiment consists of multiple Ground Stations (GSs) that receive signals from the satellite. Each GS is equipped with external time and frequency markers, provided by a custom-built module of the ESTCube-2 team, which are time-synchronised using the GPS. The precise time and frequency markers generator modules will inject the signal to the GS receiver input, together with the received signal from the satellite. The RF signal, along with injected time and frequency markers, will be recorded at each participating GS, and recordings will be forwarded to a data-processing node where time of arrival can be calculated for each received packet. A modular approach is implemented, as no significant changes in the GS hardware are required as long as the station has RF-recording capability; therefore more GSs can be included later on as well.

The experiment requires the satellite to continuously transmit data during an entire pass and GSs to receive multiple data packets. One can obtain the location coordinates of the satellite and the time by triangulation, which is

achieved by correlating signals of multiple GSs. At least five GSs are required in order to obtain decently-accurate location coordinates. Additional GSs would naturally improve accuracy.

It becomes comparatively easier to track a satellite with known altitude and position – a two-line element-based approach is already sufficient for tracking (for communication purposes); however, the absolute position in space is known with an accuracy of a few kilometres. The change in altitude can be analysed for both natural aerodynamic drag and CDP-induced change in altitude. Change in orbit can be measured by calculating the Doppler shift and difference in the time-of-signal packet received at each GS. Triangulation can be conducted once a week in order to determine the deorbiting rate, which would greatly improve the altitude/time resolution compared to the SGP model, which uses two-line elements as an orbital parameter input.

4.4. ESTCube-2 bus and other payloads

The ESTCube-2 bus consists of the OBC for telemetry handling, data logging and storage; the Electrical Power System (EPS) for power collection, storage and distribution, including Side Panels (SPs) for power harvesting; the Communication system (COM) for telemetry; ST; and AOCS (see Subsection 4.1). The aforementioned subsystems are integrated into a $96\times96\times60$-mm^3 volume. The bus schematic is shown in Figure 10.

The OBC handles the operations of all subsystems and payloads, runs the AOCS algorithms and stores housekeeping and telemetry data. The central computer of the satellite is an STM32F767II, which is an ARM-Cortex-M7-based MCU. The MCU features 512 kB of Static Random-Access Memory (SRAM) and 2 MB of a flash memory. At least two images of firmware are stored on the processor for redundancy. The OBC is at the centre of all internal communications; the avionics stack is connected via three Internal Communication Protocol (ICP) buses, and the payloads are connected via two Cubesat Space Protocol (CSP) buses.

SPs host antennas and the Corrosion-Resistance Experiment (CRE) on the

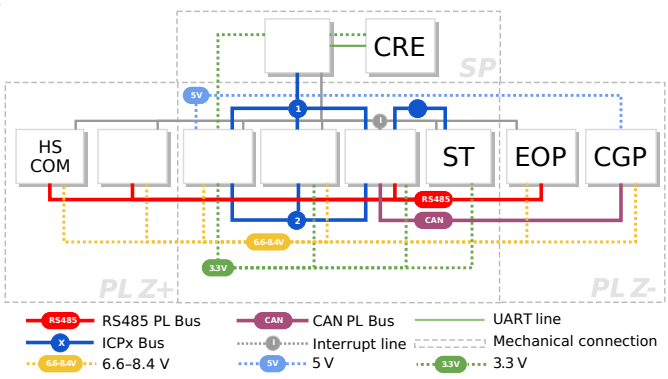

Figure 10: Overview of the ESTCube-2 bus.

+x side and provide an opening for the Earth-Observation Payload (EOP) (+x side), electron emitters (+x side) and the ST (−x side) (Figure 8).

The EOP is a multispectral imaging system comprising of two single-band imagers based on the European Student Earth Orbiter (ESEO) secondary camera [46]. The cameras use COTS Zeiss Sonnar T* optics with a focal length of 50 mm and F/1.5 aperture. The sensor is the MT9P031 (from *ON Semiconductor*), which is a CMOS sensor with a 2.2-μm pixel pitch. The imager has a 9.56° diagonal FoV and ground-sampling distances of about 22 m and 31 m at altitudes of 500 km and 700 km, respectively, both cases without possible smearing. The diameter of the ideal diffraction image is 1.4 times smaller. The spectral bands are 857 nm and 660 nm, both with 30 nm full width at half maximum, which are implemented with *Semrock* bandpass filters from the *BrightLine HC* series.

The High-Speed-COMmunication system (HSCOM) is an FPGA-based (reprogrammable in orbit) SDR-type transceiver, which supports the use of variable envelope modulation schemes in nanosatellites. The main objectives of the payload are to ensure a high-data-rate downlink channel for data collected by on-board payloads and to evaluate the use of dynamic adaptive coding and modulation modes in nanosatellites' communications systems. The HSCOM operates in amateur-radio-frequency bands: the 5830–5850 MHz band for downlink

(up to 25 Mbps) and 5650–5670 MHz band for uplink.

A compact CRE module has been designed to study the corrosion of materials and protective coatings in LEO caused by ATOX, as well as to study the radiation-shielding efficiency of multilayered smart materials. The module is partially external, with the tested materials sitting outside the satellite and exposed to the space environment, while the measurement electronics and radiation sensors are placed inside. The CRE will be carried out with two aluminium wires (diameter 250 μm) wrapped around a holder; one of these wires will be coated with a patented nanostructured ceramic coating [47]. The corrosion behaviour of the wires will be monitored by measuring their electrical resistance [48]. It is estimated that the uncoated aluminium wire will be oxidised and eroded due to interaction with the high-velocity ATOX, causing a decrease in its conductive cross-sectional area and, therefore, an increase in its electrical resistance (10–50 mΩ over the 2-year mission). Additionally, a custom multilayered material will be evaluated for radiation shielding efficiency; the first outer layer reduces the energy and intensity of secondary radiation created by high-velocity charged particles, and the next layer consists of multiple sublayers that absorb high-energy electromagnetic radiation.

The CubeMAG magnetometer on-board ESTCube-2 will be used to measure magnetic-field fluctuations at exospheric altitudes. Earlier ground-based measurement studies showed continuous magnetic fluctuations that are mainly due to auroral substorms, ground pulsations and geomagnetic storms [49]. Continuous magnetic measurements by the CubeMAG are aimed above the auroral oval during both quiet and strongly disturbed geomagnetic conditions. The Sun is known to be the ultimate source of the fluctuations, but disturbance transfer to ionospheric and atmospheric altitudes is not known in detail [50]. The instrument is based on the three-axis magnetic sensor hybrid (*Honeywell* HMC1001 and HMC1002), with a total instrument mass of 6 g and sensor dimensions 18.9×26.6×11.5 mm^3. The analogue-to-digital converter sample rate is 1 kS·s^{-1}, the peak power consumption is 240 mW, and the average power during measurement sessions is less than 50 mW. For separating the magnetic

fluctuations from external and internal sources, calibration magnetometers are placed in each side of the satellite. The magnetic data, acquired for full orbits (data rate <1 MB per orbit), are used to calibrate the instrument and examine, over time, how these magnetic disturbances evolve.

5. FORESAIL-1

FORESAIL-1 is the first in the FORESAIL mission series developed by the Finnish Centre of Excellence for Sustainable Space [51]. The centre is led by the University of Helsinki, and the satellite platform is being developed by Aalto University. The FORESAIL subsystems have been designed to sustain high radiation dose levels and be adaptable for operation in LEO, geostationary transfer orbit and deep space. The FORESAIL-1 layout is shown in Figure 11. The satellite is planned to be launched into LEO in 2020. In addition to deorbiting demonstration, the satellite carries several other experiments that are briefly described in this section.

- Demonstrate a retroreflector for accurate orbit determination, which can be used to estimate the deorbiting rate and track the satellite after the mission lifetime (Aalto University).
- Measure radiation belt losses using the PArticle TElescope (PATE) (University of Turku).
- Test a magnetometer, which could be used in the FORESAIL-2 mission (Aalto University). See Section 6 for more details on FORESAIL-2.
- Prepare the platform for the high-radiation FORESAIL-2 mission (Aalto University).

5.1. Attitude determination and control

The ADCS is responsible for ensuring correct attitude modes during different operation phases. The common requirement of FORESAIL-1 experiments is to

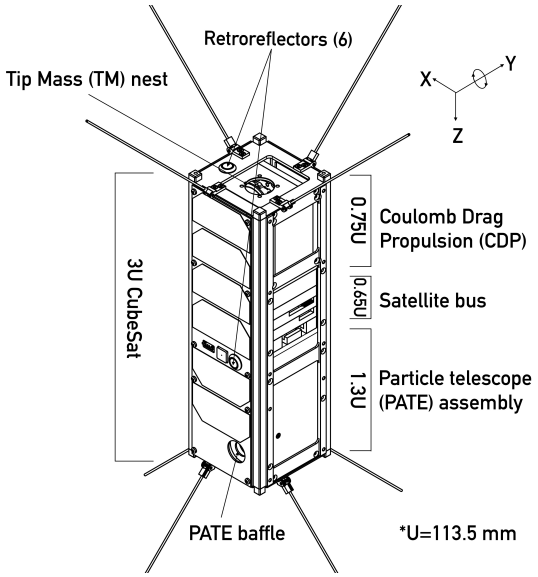

Figure 11: FORESAIL-1 anatomy.

spin the satellite, with its rotation axis pointed to different directions depending on the payload requirements. To achieve this, FORESAIL-1 is equipped with three-axis magnetorquers as the only actuators as well as three-axis gyroscopes, three-axis magnetometers and Sun sensors for attitude determination. The magnetorquers are designed to produce a maximum magnetic moment of 0.2 A·m^2 on the axes along the two short sides of the satellite and 0.1 A·m^2 on the axis along the longer side of the satellite.

The CDP payload's most demanding requirement is the total momentum required for spinning-up the satellite in order to reel out the tether while maintaining the required tether tension. The satellite's moment of inertia increases significantly as the tether is reeled out. Besides spinning-up, a spin-down control is required because the tether needs to be reeled back in to continue observations with PATE.

Figure 12 shows a possible tether-deployment strategy to maintain the allowed tether tension (see Section 2.1) during a 40-m tether deployment. The solid lines represent the minimum and maximum angular rates based on the

upper and lower tether tension limits, while the dashed lines show the angular rate of satellite as the tether is reeled out given different initial angular rates. To reel out 40 metres of the tether, we need to spin-up with the total momentum equivalent to spinning-up the satellite to 1100 deg·s^{-1} before deployment. However, the upper tension limit is exceeded during the first 20 m in such a strategy. Hence, initial deployment of the first 11 m is executed by spinning-up the satellite to 130 deg·s^{-1} with subsequent spin-up manoeuvres afterwards executed either by the CDP force itself or the ADCS, both of which require further study.

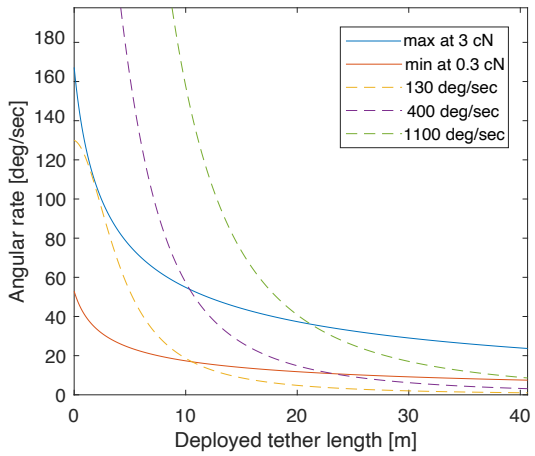

Figure 12: FORESAIL-1 initial tether-deployment strategy.

Magnetorquers can only produce torque in the plane perpendicular to the ambient magnetic field, and thus rely on variation in periodicity of the Earth's magnetic field direction in polar orbit to provide full controllability across all three axes [52]. Attitude control for a spin-stabilised satellite with only a magnetic actuator has been developed previously [53, 54, 55] and is applied to FORESAIL-1. Figure 13 shows the simulation result of spinning-up the satellite from a detumbled condition to a spin rate of 130 deg·s^{-1} around the y-axis. Figure 14 shows the pointing error of the y-axis itself and the actual spin axis during the same spin-up sequence, which is controlled to align with the z-axis of the inertial frame (coordinate system in accordance with Figure 11).

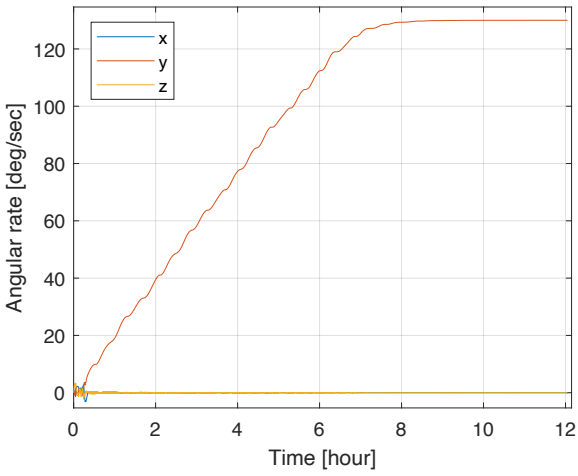

Figure 13: FORESAIL-1 angular rate during initial spin-up for 11-m tether deployment.

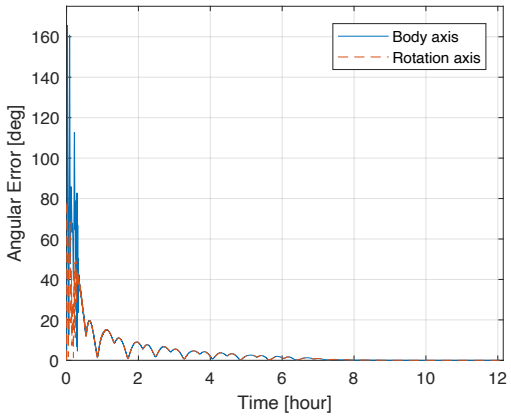

Figure 14: FORESAIL-1 pointing error during initial spin-up control.

5.2. Retroreflector

The retroreflector, also known as a corner cube prism, on board FORESAIL-1 comes with an aluminium enclosure. The retroreflector is attached to its enclosure with epoxy and occupies a $25\times14\times10$-mm^3 space. The entire assembly is attached to the outer frame of the satellite with two screws (see Figure 11). There are six retroreflectors on the satellite, one for each side.

The main objective of the retroreflectors is the orbit determination of the

satellite. It is achieved with ground-based laser ranging, where, ideally, two stations observe FORESAIL-1 simultaneously. The planned wavelength of the centre frequency is 532 nm.

The orbital data is used to estimate the deorbiting rate caused by the plasma brake. Additionally, the retroreflectors provide high-accuracy orbital tracking after the mission lifetime of a satellite. This helps to track non-operational satellites in orbit and reduce the uncertainty of collision predictions with other space assets. It also serves as a tool that helps to simulate the atmospheric re-entry of bigger objects.

5.3. FORESAIL-1 bus and other payloads

The avionics stack of the FORESAIL-1 satellite consists of necessary subsystems attached together using 52-pin stack connectors; it is housed in the aluminium enclosure.

The EPS consists of body-mounted solar panels, power-conditioning, power-distribution and battery units [56, 57]. The solar panels are mounted on every long side of the satellite. The power-conditioning unit consists of four parallel buck converters, each performing Maximum Power Point Tracking (MPPT) on its respective solar panel.

The OBC is based on a radiation-hardened ARM-Cortex-R4 core Hercules MCU. It is responsible for computation, communication and data retention, running the ADCS algorithms, operational work during CDP and PATE operations, and collecting all relevant telemetry data for downlink [57]. For fault tolerance, the OBC houses two cold redundant symmetric processors. Only one of the processors is active and powered. The arbiter switches the control to the redundant processor in the case of a failure.

The telemetry, tracking and command subsystem operates at 437.125 MHz in the Ultra-High Frequency (UHF) band for both uplink and downlink. The design consists of an MCU and two cold redundant transceivers with dedicated transmission and reception paths [58]. A UHF band turnstile antenna attached to the satellite structure connects to the transceiver board using a single connec-

tor. The subsystem consists of a CC1125 transceiver (from *Texas Instruments*) with a maximum output power of 15 dBm (30 mW), and an external power amplifier (RF5110G from *Qorvo*) to amplify the power to the desired 1.5 W in the transmit chain. In the receive chain, the subsystem consists of a low-noise amplifier and a band-pass filter.

The PATE on board FORESAIL-1 is an assembly consisting of two collimated stacks of solid-state detectors, sensitive to electrons (at 80–800 keV), protons (at 0.3–10 MeV), and neutral hydrogen atoms (at 0.3–10 MeV). The two solid-state telescopes are mounted at right angles to each other: one viewing along the rotation axis of the spacecraft and the other scanning the sky as the satellite is rotating, thus providing a measurement of pitch-angle distributions of charged particles. The main objectives of the PATE are (i) to measure the flux of electrons with a good pitch-angle resolution to separate precipitating and trapped populations, and (ii) to determine the flux of hydrogen from the solar direction, which enables measurement of energetic neutral solar atoms using the geomagnetic field as a filter. The instrument has a mass of 1.0 kg, a power consumption of about 2.5 W, and outer dimensions of $14.4 \times 9.4 \times 9.4$ cm^3. The energy resolution of the flux channels is $\Delta E/E \approx 40\%$, the time resolution is 15 s, and the angular resolution is 10°.

The magnetometer design is based on an anisotropic magnetoresistance technology and employs two sensors (*Honeywell* HMC1001 and 1002). The measurement system of the magnetometer implements a feedback loop and flipping technique for extrinsic and intrinsic noise cancellation, using an analogue-to-digital converter to measure the bridge output, a digital-to-analogue converter to set the offset-strap current, and an MCU to control the system. The existing prototype has been designed for a limited power budget, and it consumes less than 100 mW, while having a noise floor close to the noise limit of the sensor. It works in a field strength up to 20 μT, and the design can be further modified for higher strengths, if required.

6. Future prospects and scaling

6.1. Coulomb drag demonstration in various plasma environments and solar wind

The upcoming demonstration missions include i) FORESAIL-2 to characterise the Coulomb drag force depending on various plasma parameters and ii) a mission to the solar wind to demonstrate the electric sail in its authentic environment. The FORESAIL-2 mission is currently being designed by the Finnish Centre of Excellence for Sustainable Space. It will demonstrate the feasibility to utilise and characterise a nanosatellite and its instruments for scientific purposes in a high-radiation environment. While the primary objectives are related to the Ultra-Low Frequency (ULF) wave characterisation using a magnetometer and the relativistic electron and proton experiment, the Coulomb drag experiment can contribute by estimating the plasma density. This is done by measuring the tether current, which in turn characterises the capacitance of the tether with respect to the surrounding plasma. Plasma-density measurements will provide deterministic information as to whether the spacecraft is inside or outside the plasmasphere. Since ULF characterisation requires measurements to be taken at altitudes up to five Earth radii in distance, such diverse plasma environments can be used to characterise the relationship between the Coulomb drag force and plasma density from the ionosphere to the outside of plasmasphere, as well as to characterise the relationship between the Coulomb drag force and the tether voltage.

Roadmaps for both teams include demonstrating the electric sail in the solar wind, and an independent team has proposed possible translunar trajectories around or beyond the Moon's orbit [59]. Due to the complexity and cost of such a mission, it will likely be a collaborative effort between FORESAIL, ESTCube and other teams. Mission design and technology development remains in the realm of our future work.

6.2. Coulomb drag propulsion for deorbiting

The CDP payload has been designed for experimental purposes. If the in-orbit results correspond to the results and predictions of simulations, the system will be considered for larger satellite (above 500 kg) and higher orbital altitude (up to 1200 km) customisation. Taking into account the thrust (Equation 1), higher thrust can be achieved by increasing the effective Debye length, which corresponds to the number and length of tethers, as well as their voltage. The tether voltage is a somewhat limiting factor, as it is driven by the field-emission restriction point that adds an ionic current gathered by the tether and consequently increases the power consumption [34]. The limitation of the number of tethers is determined by the deployment method, and restriction of the length by the manufacturing and collision risk. The main requirement for such a payload is to be independent, meaning the system must be able to decrease the orbital altitude of the spacecraft in the case of a failure or at the end of a mission without requiring satellite subsystems to be functional, except for basic pointing ADCS manoeuvres in the initial phase.

Centrifugal deployment is not preferred for operational missions and would require a fully-functional spacecraft and its ADCS. The tether can be deployed by a miniature CGP or electrospray thruster on its tip, which makes deployment more complex, consequently increasing the price and decreasing the reliability of the system. A gravity-gradient-stabilised tether attached to a short tape tether, that is initially deployed by the spring, has been studied previously [37]. This study showed the feasibility of such an independent system that is limited to two tethers – one deployed downwards (towards Earth) and the other upwards (to higher altitudes in relation to the satellite). The downward tether will be stretched by the gravity gradient and the upward tether by a higher orbital speed. The deorbiting time of a satellite equivalent to SpaceX's Starlink (150 kg) or OneWeb (227 kg) from a 1200-km altitude is under 25 years, including the margin with the 5-km tether system. It has been estimated that a 200-kg object can be deorbited from a 1200-km altitude, and an 800-kg satellite from a 850-km altitude in 11 years [37]. However, this value largely depends on the exact

orbital parameters and the space weather, as discussed in Subsection 3.1.

6.3. Coulomb drag propulsion for interplanetary voyage

The propulsion effect of CDP depends on the length and the number of tethers. An interplanetary spacecraft would require an electron emitter to keep the tether's bias positive in order to operate in the solar-wind environment. While complex multi-tethered concepts have been discussed in the past [60, 61, 62], covering missions to non-Keplerian orbits as well as inner- and outer-Solar-system rendezvous and flybys, the latest study shows the feasibility of a fleet of autonomous nanospacecraft to reach the main asteroid belt and return to Earth's vicinity with a single 20-km tether in 3.2 years [41]. Analyses show that cubesat-esque nanospacecraft could indeed perform surface and trajectory reconstructions as well as provide spectral information on asteroids with shape reconstruction possible during a 300-km flyby [42].

7. Conclusions

This paper presents a novel deorbiting method based on Coulomb Drag Propulsion (CDP) for satellites in Low Earth Orbit (LEO). The experiment will be carried out by two independent three-unit cubesat missions – ESTCube-2 and FORESAIL-1. The thrust will be estimated in spin-rate modification mode and by decreasing the orbital altitude. The change in spin rate will be measured by the attitude determination and control system and is expected to be $\approx$0.1 deg·s^{-1} during one polar pass, in which the experiment is performed. The deorbiting rate over 10 km can be determined from the orbital elements over a period of six months. More precise orbit determination includes a radio-frequency ranging experiment for ESTCube-2 and a retroreflector for FORESAIL-1. While each satellite is equipped with a 300-m-long tether, as a conservative minimum, the estimated spin-rate change is given for deploying the first 11 metres and the deorbiting rate for a 30-m tether. The performance improves as more tether is deployed.

Key aspects of CDP deorbiting have been demonstrated in this paper: i) system requirements, deployment and operations; ii) technologies for CDP, including the tether, deployment mechanism and high-voltage source; iii) the system performance and risks. The paper briefly describes missions and other payloads of each cubesat. Roadmaps are drawn for positive CDP demonstration, known as the electric sail, in its authentic environment – the solar wind. The FORESAIL team is preparing a high-radiation-tolerant platform and instrumentation to characterise the Coulomb drag in various plasma environments on board FORESAIL-2. The ESTCube team is preparing to demonstrate (i) the electron emitters, required by the electric sail, (ii) attitude and orbit control, and (iii) communications, all adoptable for deep-space nanospacecraft operations.

Acknowledgements

The Finnish Centre of Excellence in Research of Sustainable Space is developing and will launch FORESAIL-1 and FORESAIL-2 missions, as well as designing the FORESAIL-3 mission for the solar wind. The Centre is funded through the Academy of Finland with grant numbers 312351, 312356, 312357, 312358, and 312390.

The authors would like to thank volunteers and industry partners who have contributed to the development of ESTCube-2. The research for this article was partly supported by the University of Tartu ASTRA project 2014-2020.4.01.16-0029 KOMEET "Benefits for Estonian Society from Space Research and Application", financed by the EU European Regional Development Fund. The contributions of Ahti Heinla, Priit Salumaa and more than 500 crowdfunding backers are very much appreciated for largely funding ESTCube-2 [63]. The ESTCube-2 magnetometer team acknowledges its funding by FIRI/G-EPOS (293488, 311714), Resolve Centre of Excellence (272157, 307411) and Aalto infrastructure funding.

Aalto University and its Multidisciplinary Institute of Digitalisation and Energy are thanked for Aalto-1 project funding, as are Aalto University, Nokia,

SSF, the University of Turku and RUAG Space for supporting the launch of Aalto-1.

Captain Corrosion OÜ funded the development of the materials-testing module, receiving additional funding from Enterprise Estonia Development Voucher (Project EU51950), and support from Hedgehog OÜ, who contributed to the development of the required electronics. The Laboratory of Thin Film Technology, Institute of Physics, University of Tartu prepared the coating for the Al-wire, and also purchased the wire and its holder with the help of Estonian-Ministry-of-Education-and-Science-funded projects IUT2-24 and TK141.

References

References

[1] R. Corfield, Sputnik's legacy: the drama that led to the Soviet Union's launch 50 years ago this month of the first artificial satellite – Sputnik 1, Physics world (10) (2007) 23.
URL https://iopscience.iop.org/article/10.1088/2058-7058/20/10/30/meta

[2] A. Darya, I. Fernini, Analysis of Space Debris Re-Entry over the Arabian Peninsula (2004 to 2018), in: 2018 International Conference on Signal Processing and Information Security (ICSPIS), 2018. doi:10.1109/CSPIS.2018.8642726.

[3] Inter-Agency Space Debris Coordination Committee, Stability of the Future LEO Environment, IADC-12-08 Rev.1 (2013) 22.
URL https://www.iadc-online.org/Documents/IADC-2012-08,%20Rev%201,%20Stability%20of%20Future%20LEO%20Environment.pdf

[4] T. Wang, Analysis of Debris from the Collision of the Cosmos 2251 and the Iridium 33 Satellites, Science and global security (2) (2010) 87. doi:10.1080/08929882.2010.493078.

[5] H. Krag, M. Serrano, V. Braun, P. Kuchynka, M. Catania, J. Siminski, M. Schimmerohn, X. Marc, D. Kuijper, I. Shurmer, A. O'Connell, M. Otten, I. Muñoz, J. Morales, M. Wermuth, D. McKissock, A 1-cm space debris impact onto the Sentinel-1A solar array, Acta Astronautica 137 (2017) 434–443. doi:10.1016/j.actaastro.2017.05.010.

[6] B. B. Virgili, J. Dolado, H. Lewis, J. Radtke, H. Krag, B. Revelin, C. Cazaux, C. Colombo, R. Crowther, M. Metz, Risk to space sustainability from large constellations of satellites, Acta Astronautica 126 (2016) 154 – 162. doi:10.1016/j.actaastro.2016.03.034.

[7] J. Radtke, C. Kebschull, E. Stoll, Interactions of the space debris environment with mega constellations – Using the example of the OneWeb constellation, Acta Astronautica 131 (2017) 55 – 68. doi:10.1016/j.actaastro.2016.11.021.

[8] S. L. May, S. Gehly, B. Carter, S. Flegel, Space debris collision probability analysis for proposed global broadband constellations, Acta Astronautica 151 (2018) 445 – 455. doi:10.1016/j.actaastro.2018.06.036.

[9] I. del Portillo, B. G. Cameron, E. F. Crawley, A technical comparison of three low earth orbit satellite constellation systems to provide global broadband, Acta Astronautica 159 (2019) 123 – 135. doi:10.1016/j.actaastro.2019.03.040.

[10] Space Exploration Holdings, LLC, Application for Approval for Orbital Deployment and Operating Authority for the SpaceX V-band NGSO Satellite System, IBFS File No. SAT-LOA-20170301-00027, FCC Boosts Satellite Broadband Connectivity & Competition FCC 18-161 (2018) 2.
URL https://docs.fcc.gov/public/attachments/FCC-18-161A1.pdf

[11] C. Niederstrasser, Small Launch Vehicles – a 2018 State of the Industry Survey, in: 32^{nd} Annual AIAA/USU Conference on Small Satellites, SSC18-IX-01, 2018, pp. 4–10.

URL https://digitalcommons.usu.edu/cgi/viewcontent.cgi?article=4118&context=smallsat

[12] H. Klinkrad, P. Beltrami, S. Hauptmann, C. Martin, H. Sdunnus, H. Stokes, R. Walker, J. Wilkinson, The ESA Space Debris Mitigation Handbook 2002, Advances in Space Research 34 (5) (2004) 1251 – 1259. doi:10.1016/j.asr.2003.01.018.

[13] C. P. Mark, S. Kamath, Review of Active Space Debris Removal Methods, Space Policy 47 (2019) 194 – 206. doi:10.1016/j.spacepol.2018.12.005.

[14] P. M. Waswa, M. Elliot, J. A. Hoffman, Spacecraft Design-for-Demise implementation strategy & decision-making methodology for low Earth orbit missions, Advances in Space Research 51 (2013) 1627 – 1637. doi:10.1016/j.asr.2012.11.020.

[15] M. Trisolini, H. G. Lewis, C. Colombo, Spacecraft design optimisation for demise and survivability, Aerospace science and technology 77 (2018) 638 – 657. doi:10.1016/j.ast.2018.04.006.

[16] R. Biesbroek, L. Innocenti, A. Wolahan1, S. M. Serrano, e.Deorbit – ESA's Active Debris Removal Mission, in: 7^{th} European Conference on Space Debris, published by the ESA Space Debris Office, Ed. T. Flohrer & F. Schmitz, June 2017, pp. 1–10.
URL http://spacedebris2017.sdo.esoc.esa.int

[17] A. Messidoro, L.Marconi, M. Conte, A. Chiesa, G. Gambacciani, L. Maffioli, K. Wormnes, S. Aziz, TETHERS AS PULLING CAPTURE TECHNOLOGY FOR E.DEORBIT AND NET/HARPOON-BASED ADR MISSIONS, in: 7^{th} European Conference on Space Debris, Darmstadt, published by the ESA Space Debris Office, Ed. T. Flohrer & F. Schmitz, June 2017, pp. 1–13.
URL http://spacedebris2017.sdo.esoc.esa.int

[18] J. L. Forshaw, G. S. Aglietti, T. Salmon, I. Retat, M. Roe, C. Burgess, T. Chabot, A. Pisseloup, A. Phipps, C. Bernal, F. Chaumette, A. Pollini, W. H. Steyn, Final payload test results for the RemoveDebris active debris removal mission, Acta Astronautica 138 (2017) 326 – 342. doi:10.1016/j.actaastro.2017.06.003.

[19] L. Orsini, L. Niccolai, G. Mengali, A. A. Quarta, Plasma brake model for preliminary mission analysis, Acta Astronautica 144 (2018) 297 – 304. doi:10.1016/j.actaastro.2017.12.048.

[20] R. Hoyt, T. Unlimited, Inc., Terminator Tape: A Cost-Effective De-Orbit Module for End-of-Life Disposal of LEO Satellites, AIAA SPACE 2009 Conference & Exposition AIAA SPACE Forum. doi:10.2514/6.2009-6733.

[21] C. Underwood, A. Viquerat, M. Schenk, B. Taylor, C. Massimiani, R. Duke, B. Stewart, S. Fellowes, C. Bridges, G. Aglietti, B. Sanders, D. Masutti, A. Denis, InflateSail De-Orbit Flight Demonstration Results and Follow-On Drag-Sail Applications, in: 69^{th} International Astronautical Congress, IAC-18-A6.5.2, 2018, pp. 1–16.
URL https://goo.gl/JBbMsR

[22] M. Murbach, P. Papadopoulos, C. Glass, A. Dwyer-Cianciolo, R. Powell, S. Dutta, A. Guarneros-Luna, F. Tanner, A. Dono, Modeling the Exo-Brake and the Development of Strategies for De-Orbit Drag Modulation, in: 13^{th} International Planetary Probe Workshop, June 2016, p. 20.
URL https://ntrs.nasa.gov/search.jsp?R=20160008903

[23] P. Janhunen, Electrostatic plasma brake for deorbiting a satellite, Journal of Propulsion and Power 26 (2) (2010) 370–372. doi:10.2514/1.47537.

[24] I. Iakubivskyi, H. Ehrpais, A. Slavinskis, H. Kuuste, I. Sünter, E. Ilbis, E. Oro, J. Kütt, P. Janhunen, P. Toivanen, J. Envall, ESTCube-2 plasma brake payload for effective deorbiting, in: 7^{th} European Conference on Space Debris, published by the ESA Space Debris Office, Ed. T. Flohrer &

F. Schmitz, June 2017, pp. 1–7.
URL http://spacedebris2017.sdo.esoc.esa.int

[25] K. D. Bunte, T. Sinn, A. Riemer, R. Hahn, P. Seefeldt, T. Spröwitz, M. Sznajder, Sustainability of drag-augmentation devices, Presentation given at CleanSpace Industrial Days at ESA/ESTEC (2016) 6–7.
URL https://indico.esa.int/event/128/attachments/737/905/03_Bunte_etal_Sustainability_CID_01_00.pdf

[26] A. Slavinskis, M. Pajusalu, H. Kuuste, E. Ilbis, T. Eenmäe, I. Sünter, K. Laizans, H. Ehrpais, P. Liias, E. Kulu, et al., ESTCube-1 in-orbit experience and lessons learned, IEEE Aerospace and Electronic Systems Magazine 30 (8) (2015) 12–22. doi:10.1109/MAES.2015.150034.

[27] O. Khurshid, T. Tikka, J. Praks, M. Hallikainen, Accommodating the plasma brake experiment on-board the Aalto-1 satellite., Proceedings of the Estonian Academy of Sciences 63 (2014) 258–266. doi:10.3176/proc.2014.2S.07.

[28] B. S. Yu, H. Wen, D. P. Jin, Review of deployment technology for tethered satellite systems, Acta Mechanica Sinica 34 (4) (2018) 754–768. doi:10.1007/s10409-018-0752-5.

[29] P. Janhunen, Electric sail for spacecraft propulsion, Journal of Propulsion and Power 20 (4) (2004) 763–764. doi:10.2514/1.8580.

[30] P. Janhunen, Boltzmann electron PIC simulation of the E-sail effect, Annales Geophysicae 33 (2015) 1507–1512. doi:10.5194/angeo-33-1507-2015.

[31] J. Envall, P. Toivanen, P. Janhunen, Thin multi-wire Coulomb Drag Tether by Diffusion Bonding, in: The Sixth International Conference on Tethers is Space, Madrid, June 12-14, Spain, 2019, p. 15.

[32] D. Bock, M. Tajmar, Highly miniaturized FEEP propulsion system (NanoFEEP) for attitude and orbit control of CubeSats, Acta Astronautica 144 (2018) (2018) 422–428. doi:10.1016/j.actaastro.2018.01.012.

[33] M. Tajmar, Survey on FEEP Neutraliser Options, 38^{th} AIAA/ASME/SAE/ASEE Joint Propulsion Conference & Exhibit. AIAA 2002-4243. doi:10.2514/6.2002-4243.

[34] P. Janhunen, Simulation study of the plasma-brake effect, Annales Geophysicae 32 (2014) 1207–1216. doi:10.5194/angeo-32-1207-2014.

[35] S. Lätt, A. Slavinskis, E. Ilbis, U. Kvell, K. Voormansik, E. Kulu, M. Pajusalu, H. Kuuste, I. Sünter, T. Eenmäe, et al., ESTCube-1 nanosatellite for electric solar wind sail in-orbit technology demonstration, Proceedings of the Estonian Academy of Sciences 63 (2S) (2014) 200–209. doi:10.3176/proc.2014.2S.01.

[36] W. Dong, Z. Chang-yin, An Accuracy Analysis of the SGP4/SDP4 Model, Chinese Astronomy and Astrophysics 34 (1) (2010) 69–76. doi:10.1016/j.chinastron.2009.12.009.

[37] P. Janhunen., P. Toivanen, K. Ruosteenoja, Electrostatic tether plasma brake, ESA CleanSat Building Block 15 (BB15) final report (January 18, 2017) 1–67.
URL http://www.electric-sailing.fi/papers/BB15-LSIversion-with-execsum.pdf

[38] H. Ehrpais, I. Sünter, E. Ilbis, J. Dalbins, I. Iakubivskyi, E. Kulu, I. Ploom, P. Janhunen, J. Kuusk, J. Sate, R. Trops, A. Slavinskis, ESTCube-2 mission and satellite design, in: The 4S Symposium, 2016.
URL https://www.researchgate.net/publication/303974831

[39] I. Iakubivskyi, H. Ehrpais, J. Dalbins, E. Oro, E. Kulu, J. Kütt, P. Janhunen, A. Slavinskis, E. Ilbis, I. Ploom, I. Sünter, R. Trops, M. Merisalu, ESTCube-2 mission analysis: Plasma brake experiment for deorbiting, in:

67^{th} International Astronautical Congress, IAC-16.E2.4.4.x33190, 2016. URL https://www.researchgate.net/publication/308054281

[40] A. Slavinskis, E. Kulu, J. Viru, R. Valner, H. Ehrpais, T. Uiboupin, M. Järve, E. Soolo, J. Envall, T. Scheffler, et al., Attitude determination and control for centrifugal tether deployment on the ESTCube-1 nanosatellite., Proceedings of the Estonian Academy of Sciences 63 (2014) 242–249. doi:10.3176/proc.2014.2S.05.

[41] A. Slavinskis, I. Iakubivskyi, P. Janhunen, P. Toivanen, K. Muinonen, A. Penttilä, M. Granvik, T. Kohout, M. Gritsevich, M. Pajusalu, I. Sünter, et al., Nanospacecraft fleet for multi-asteroid touring with electric solar wind sails, in: IEEE Aerospace Conference, 2018. doi:10.1109/AERO.2018.8396670.

[42] M. Pajusalu, A. Slavinskis, Characterization of Asteroids Using Nanospacecraft Flybys and Simultaneous Localization and Mapping, in: 2019 IEEE Aerospace Conference, 2019, pp. 1–9. doi:10.1109/AERO.2019.8741921.

[43] J. E. Riedel, S. Bhaskaran, S. Desai, D. Han, B. Kennedy, G. Null, S. Synnott, T. Wang, R. Werner, E. Zamani, T. McElrath, D. Han, M. Ryne, Autonomous Optical Navigation (AutoNav), Deep Space 1 Technology Validation Report, Tech. rep., Jet Propulsion Laboratory, California Institute of Technology, Pasadena, California (2002). URL https://pdssbn.astro.umd.edu/holdings/ds1-c-micas-3-rdr-visccd-borrelly-v1.0/document/doc_Apr04/int_reports/AutoNav_Integrated_Report_A.pdf

[44] B. Segret, D. Hestroffer, G. Quinsac, M. Agnan, J. Vannitsen, B. Mosser, In-Flight Orbit Determination for a Deep-Space CubeSat, in: IEEE Aerospace Conference, 2018. doi:10.1109/AERO.2018.8396756.

[45] J. Dalbins, et al., Alternative communications approach to deep-space missions, in: 8^{th} Interplanetary CubeSat Workshop, 2019.

URL https://icubesat.org/papers/2019-2/2019-b-2-1-alternative-communications-approach-to-deep-space-missions/

[46] I. Sünter, H. Kuuste, A. Slavinskis, A. Agu, E. Ilbis, G. Olentšenko, I. Iakubivskyi, et al., Design and Testing of a Dual-Camera Payload for ESEO, in: 67^{th} International Astronautical Congress, B4.4.3.x31978, 2016.
URL https://www.researchgate.net/publication/308053813

[47] V. Sammelselg, L. Aarik, M. Merisalu, Method of preparing corrosion resistant coatings, Patent WO2014102758A1 (2014).
URL https://patents.google.com/patent/WO2014102758A1/en

[48] C. Britton, Introduction to Corrosion Measurement Techniques, Anti-Corrosion Methods and Materials 22 (6/7) (1975) 9–11. doi:10.1108/eb006981.

[49] E. I. Tanskanen, A comprehensive high-throughput analysis of substorms observed by IMAGE magnetometer network: Years 1993–2003 examined, Journal of Geophysical Research: Space Physics 114 (A5) (2009) 1–11. doi:10.1029/2008JA013682.

[50] E. I. Tanskanen, K. Snekvik, J. A. Slavin, D. Perez-Suarez, A. Viljanen, M. L. Goldstein, M. J. Käpylä, R. Hynönen, L. V. T. Häkkinen, K. Mursula, Solar Cycle Occurrence of Alfvénic Fluctuations and Related Geo-Efficiency, Journal of Geophysical Research: Space Physics 122 (10) (2017) 9848–9857. doi:10.1002/2017JA024385.

[51] M. Palmroth, J. Praks, R. Vainio, P. Janhunen, E. K. J. Kilpua, N. Y. Ganushkina, A. Afanasiev, M. Ala-Lahti, A. Alho, T. Asikainen, et al., FORESAIL-1 cubesat mission to measure radiation belt losses and demonstrate de-orbiting, J. Geophys. Res. Space Physics 124 (2019) 1–26. doi:10.1029/2018JA026354.

[52] S. P. Bhat, A. S. Dham, Controllability of spacecraft attitude under magnetic actuation, in: 42^{nd} IEEE International Conference on Decision and

Control (IEEE Cat. No.03CH37475), Vol. 3, 2003, pp. 2383–2388 Vol.3. doi:10.1109/CDC.2003.1272976.

[53] A. de Ruiter, A fault-tolerant magnetic spin stabilizing controller for the JC2Sat-FF mission, Acta Astronautica 68 (1) (2011) 160 – 171. doi:10.1016/j.actaastro.2010.07.012.

[54] D. Roldugin, P. Testani, Spin-stabilized satellite magnetic attitude control scheme without initial detumbling, Acta Astronautica 94 (1) (2014) 446 – 454. doi:10.1016/j.actaastro.2013.01.011.

[55] A. Slavinskis, U. Kvell, E. Kulu, I. Sünter, H. Kuuste, S. Lätt, K. Voormansik, M. Noorma, High spin rate magnetic controller for nanosatellites, Acta Astronautica 95 (2014) 218–226. doi:10.1016/j.actaastro.2013.11.014.

[56] A. Ali, M. Mughal, H. Ali, L. Reyneri, Innovative power management, attitude determination and control tile for CubeSat standard NanoSatellites, Acta Astronautica 96 (2014) 116 – 127. doi:10.1016/j.actaastro.2013.11.013.

[57] M. R. Mughal, A. Ali, L. M. Reyneri, Plug-and-play design approach to smart harness for modular small satellites, Acta Astronautica 94 (2) (2014) 754 – 764. doi:10.1016/j.actaastro.2013.09.015.

[58] H. Ali, A. Ali, M. R. Mughal, L. Reyneri, C. Sansoe, J. Praks, Modular Design of RF Front End for a Nanosatellite Communication Subsystem Tile Using Low-Cost Commercial Components, International Journal of Aerospace Engineering 2019 (2019) 11. doi:10.1155/2019/8174158.

[59] L. Niccolai, A. A. Quarta, G. Mengali, F. Petrucciani, Possible Trajectories for Electric Solar Wind Sail Validation, Aerotecnica Missili & Spazio 98 (2019) 1–7. doi:10.1007/s42496-019-00012-7.

[60] S. Merikallio, P. Janhunen, Moving an asteroid with electric solar wind sail, Astrophysics and Space Sciences Transactions (ASTRA) 6 (1) (2010) 41. doi:10.5194/astra-6-41-2010.

[61] P. Janhunen, P. Toivanen, J. Envall, S. Merikallio, G. Montesanti, J. G. del Amo, U. Kvell, M. Noorma, S. Latt, Overview of electric solar wind sail applications, Proceedings of the Estonian Academy of Sciences 63 (2 SI) (2014) 267–279. doi:10.3176/proc.2014.2S.08.

[62] P. Janhunen, J.-P. Lebreton, S. Merikallio, M. Paton, G. Mengali, A. A. Quarta, Fast E-sail Uranus entry probe mission, Planetary and Space Science 104 (2014) 141–146. doi:10.1016/j.pss.2014.08.004.

[63] K. Kalnina, K. Bussov, H. Ehrpais, T. Teppo, S.-K. Kask, M. Jauk, J. Envall, A. Slavinskis, Crowdfunding for satellite development: ESTCube-2 case, in: IEEE Aerospace Conference, 2018. doi:10.1109/AERO.2018.8396722.